Detailed analysis of the ice surface after binding of an insect antifreeze protein and correlation with the Gibbs-Thomson equation

Julian Gerhäuser, Volker Gaukel*

KIT (Karlsruhe Institute of Technology), Institute of Process Engineering in Life Sciences, Section I: Food Process Engineering, Kaiserstraße 12, 76131 Karlsruhe, Germany

KEYWORDS

Molecular Dynamics, AFP, antifreeze protein, Gibbs-Thomson, ice surface, curvature

ABSTRACT

Antifreeze proteins are able to influence the ice crystal growth and the recrystallization process due to the Gibbs-Thomson effect. The binding of the antifreeze protein leads to the formation of a curved ice surface and it is generally assumed that there is a critical radius between the proteins on the ice surface that determines the maximal thermal hysteresis. Up to now, this critical radius has not yet been proven beyond doubt or only in poor agreement with the Gibbs-Thomson equation. Using molecular dynamics (MD) simulations, the resulting three-dimensional surface

structure is analyzed and the location of the critical radius is identified. Our results demonstrate that the correct analysis of the geometry of ice surface is extremely important and cannot be guessed upfront the simulation. In contrary to earlier expectations from literature, we could show that the critical radius is not located directly between the adsorbed proteins. In addition, we showed that the minimum temperature at which the system does not freeze is in very good agreement with the value calculated with Gibbs-Thomson equation at the critical radius as long as dynamic system conditions are taken into account. This proves on the one hand that the Gibbs-Thomson effect is the basis of thermal hysteresis and that MD simulations are suitable for the prediction of the melting point depression.

INTRODUCTION

Several microorganisms, animals and plants inhabiting cold climates produce specialized proteins called antifreeze proteins (AFP) or ice-binding proteins (IBP). These proteins protect body fluids from cold damage[1–4]. Under subzero temperature conditions ice crystals can form in body fluids like cytoplasm, blood or haemolymph, and in the apoplast of plants[3]. This leads to serious damage within the surrounding tissue. In addition to physical damage, the formation of intracellular ice results in an increase of osmotic pressure due to the removal of liquid water and concentration of the remaining solutes[5], which causes plasmolysis and disruption of the cell integrity. For this reason, AFP are of special interest in industrial and medical applications for example as food additive in frozen meat, fish or ice cream or as cryoprotective agent during frozen storage of cells, tissues and organs[6].

AFP bind to specific planes of ice crystals and thus inhibit further ice growth during cooling to a certain extent. The resulting gap between the equilibrium melting temperature and the temperature of sudden ice growth is called thermal hysteresis (TH)[7,8]. Many authors term the

temperature of sudden ice growth the "freezing point" which is physically not correct, as ice crystals are already present when their growth is stopped by AFP. Moreover, bound AFPs are able to increase the equilibrium melting temperature of the ice crystal but in a smaller extent compared to TH[9].

Different characteristics of antifreeze proteins influence their ability to stop ice crystal growth and thereby the extent of the TH. One critical property is the ice plane bound by the AFP (Figure 1). Two types of AFP can be distinguished, moderately active and hyperactive AFP. Hyperactive AFP are able to bind to the basal plane or to the basal in combination with other planes[10,11] and are found in insects and some microorganisms[12]. Their activity is up to ten fold higher than the one of moderately active AFP, which are typically found in fish[13]. Moderately active AFP bind preferably to planes parallel to the c axis[8]. For example, winter flounder AFP binds to the pyramidal plane[14].

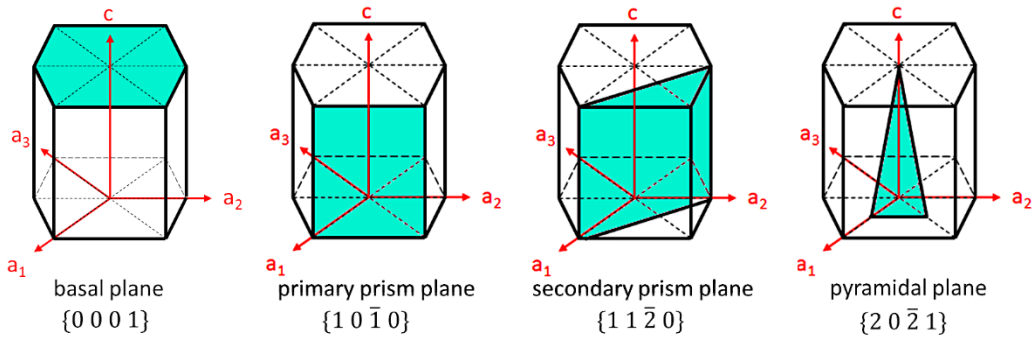

Figure 1. Possible ice binding planes for AFP. The specific plane is shown in turquoise with the corresponding miller index. Modified from [13].

Besides being able to influence the freezing and melting behavior of an ice crystal, AFPs affect the ice recrystallization. During the process of ice recrystallization, the total mass of ice crystals is constant whilst the number of crystals decrease and the mean ice crystal sizes increase[15,16] by thermodynamic reasons. The addition of AFP reduces recrystallization effects even when they are added in low concentrations[17,18].

In general, it is postulated that, due to their ability to interact with the ice crystal surface, the presence of AFP leads to a pinned surface with characteristic curvature[19] (Figure 2).

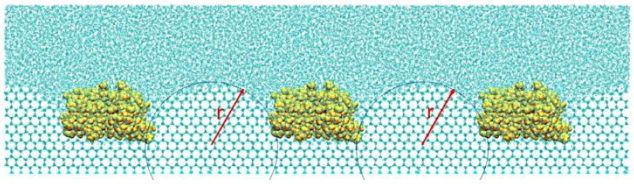

Figure 2. Curved ice surface between three antifreeze proteins (yellow). Ice can grow between the proteins and forms a curved surface. The radius r of the curvature influences the vapor pressure of the solid phase, which leads to a limitation of the ice, although a decreasing temperature.

Both effects, TH and ice recrystallization inhibition, involve the Gibbs-Thomson effect[20] (Equation 1), which describes the change of the melting temperature due to a curved surface at constant pressure. A decisive parameter here is the radius r or the diameter x = 2r of the curvature.

Equation 1. Gibbs-Thomson equation for a spherical particle

$$\Delta T_m = T_m^{\infty} - T_m(x) = \frac{4\sigma_{sl} T_m^{\infty}}{x \Delta H_f \rho_s}$$

For the calculation of the thermal hysteresis ΔT_m , which is the difference between the bulk melting temperature T_m^{∞} and the melting temperature of the ice crystal $T_m(x)$ with a diameter of size x, the surface tension σ_{sl} between the solid and liquid phase, the bulk enthalpy of fusion ΔH_f and the density of the solid ρ_s is needed. The factor of four, often referred to as geometry factor, originates from the Young-Laplace equation (Equation 2), which describes the pressure difference Δp across a curved interface.

80 **Equation 2.** Young-Laplace equation

81 $$\Delta p = -\sigma\left(\frac{1}{r_1} + \frac{1}{r_2}\right)$$

82 If a spherical particle or surface is assumed, both principal radii r_1 and r_2 are of the same length
83 and can be combined to 2/r or 4/x. This results in a geometrical factor of 4 as seen in Equation 1.
84 In the case of a cylindrical shape, one of the radii becomes infinite and therefore only the radius
85 perpendicular to the height of the cylinder has an influence. This results in 1/r or 2/x, and leads to
86 a geometric factor of two for a cylindrical shape in Equation 1. It is obvious that the value of $T_m(x)$
87 depends not only on the radius but also on the given geometry. Unfortunately, less attention is paid
88 to the latter in the literature.

89 To prove the assumption that the Gibbs-Thomson Effect leads to TH of AFP many attempts
90 have been discussed in literature. As it is impossible by direct observation to proof the existence
91 of the curvature on an AFP studded ice crystal surface, to measure the curvatures or the surface
92 allocation of the bound molecules, most studies are based on simulation results from molecular
93 dynamics (MD) studies.

94 Experimentally, the binding plane or multiple binding planes can be identified with fluorescence
95 labeled AFP[21,22] and the TH activity can be determined by differential scanning calorimetry,
96 sonocrystallization or other methods[23–25]. In addition, the ice recrystallization inhibition can be
97 quantified by several assays and optical methods[18]. An attempt to determine the surface
98 distribution of bound AFP molecules experimentally in an indirect way was described by Drori et
99 al.[26]. Fluorescence labeled *Tenebrio molitor* AFP (*Tm*AFP) bind to a single ice crystal in a
100 specialized microfluidic system. Due to the intensity of the emitted light, the number of bound
101 molecules can be determined. From these investigations, Drori et al. calculated an average distance
102 of 7 nm for a measured TH value of 0.73 K.

In contrast to experimental methods, MD simulations can deliver information about the details on a molecular level. During the last decade, MD simulations gained a lot of importance in the field of antifreeze and ice binding molecules. It is shown that the simulation results support the theory of a curved ice surface and the applicability of the Gibbs-Thomson effect[27–29]. A point that one has to keep in mind for MD simulations of AFP is that the simulations provide only information about the interaction of the AFP with one specific ice plane. Nevertheless, crystal growth is a three-dimensional process and AFP have different affinities for the different planes, which makes a direct comparison of TH between experiment and simulation unfeasible. Furthermore, it is necessary to run the simulation long enough to allow rare events to happen. These in turn can lead to overgrowth of the protein if the ice crystal surface has developed a distinctive curvature. The time period of the experiment is of course much longer than of the simulation.

A good example is provided by Naullage et al.[30]. They compared the experimental findings of Drori et al. with a MD simulation of *Tm*AFP with a distance of 7.4 nm between the centers of mass of the molecules resulting in a TH of 9 K after 100 ns of simulation time[30]. According to the large difference of TH of the experimental results Naullage et al. argued that the experimental distance is determined by averaging and statistical distribution of antifreeze molecules and that it is likely that there are also larger open spaces in between that lower the extent of TH in the experiment. In addition, the observation time in the experiment is much longer than in the simulation allowing for rare formation of ice bridges. Based on this and additional simulations, Naullage et al. suggest, "that the longest distances in the distribution control the thermal hysteresis" (Naullage et al. 2018, page 1716). This seems reasonable, because the ice radius between two bound AFP may increase with a greater distance between the bound molecules and because of this, $T_m(x)$ rises. We go along

with this argumentation and want to add that the three-dimensional aspects of ice growth and the dynamic equilibrium on the surface must be taken into account, too. Especially when it comes to the critical radius and the linkage of this radius to the Gibbs-Thomson.

Although there are publications that analyze and address these aspects but do not combine them into a complex overall picture. Kuiper et al. simulated the binding of spruce budworm (sbw) AFP to an growing ice crystal and finds that the binding of the protein to the ice surface is facilitated by ordered water molecules[28]. Moreover, this ordering seems responsible for the ice plane specificity. In addition, they calculate the radius according to the Gibbs-Thomson equation with cylindrical geometry factor and create an overlay of the curvature and the circular segment obtained. Unfortunately, it is not clear from their publication why the cylindrical geometry factor is used and why the overlay is created at the location between the sbwAFP since no complete analysis of the three-dimensional ice surface structure is shown.

Also Midya et al.[31] calculated the expected length of the radius according the Gibbs-Thomson equation and compared it with their simulations at different temperatures. However, it is not clear what geometry factor is used and where and how they measured the radius. Furthermore, the expected and calculated radii differ by at least 1.8 nm from each other. Additionally, there are several other publications that show a curved ice surface but do not link the radius of curvature with the Gibbs-Thomson equation[27,29,32].

An interesting difference between the simulations of Kuiper et al. and Midya et al. is the overall structure of the ice surface. While Midya et al. visualize a spherical or ellipsoidal curvature with the center at the intersection of the diagonals, Kuiper et al. assumes a cylindrical surface. As shown above the geometrical factor used in the Gibbs-Thomson equation is critical for the calculation of TH. As many different radii of curvature can be formed during the process of ice growth, from our

point of view, the critical location where ice starts to overgrow the AFP needs first to be identified. Second, the surface geometry at this point needs to be evaluated to identify the correct Gibbs Thomson Eq. for the calculation of TH. This illustrates the importance of knowing the structure of the ice surface and where different radii can be located.

Another important aspect is the dynamic behavior of the ice surface close to the equilibrium. Water molecules are able to join or desorb the ice lattice, which leads to a fluctuation of the surface curvature and thus its radius making a static evaluation unfavorable[28].

To accomplish these aspects in this study, radii in all directions inside the simulation box will be analyzed (Figure 5 A)) to identify the critical radius, which is decisive for the overgrowing ice front. Due to the rectangular arrangement of the AFP in the simulation (Figure 3 B)), we expect a spherical elevation in the center similar to Midya et al. to arise. As stated by Naullage et al. the longest distance should yield the critical radius, which is the diagonal direction between two AFP in our simulation setup. To our knowledge, this is the first time that the diagonal is explicitly taken in consideration and that radii in all directions within the systems are observed to identify the critical radius. Moreover, the temperature T_{Min} at which the system remains unfrozen is determined by simulating different temperatures. The ice surface in the system at T_{Min} is then analyzed in static and dynamic way and $T_m(x)$ is calculated with the Gibbs-Thomson equation. This should yield the observed T_{Min}, verifying that MD simulations can predict accurately the melting point depression in accordance with the Gibbs-Thomson equation for a given geometry.

EXPERIMENTAL

Software and simulation parameters

171 The MD simulations done with GROMACS[33] version 2019.3 are visualized and analyzed using
172 the Visual Molecular Dynamics[34] (VMD) viewer. In order to achieve realistic properties of ice and
173 the freezing process, the TIP4P/Ice water model[35] in combination with the OPLS-AA[36] force field
174 is used. This water model is based on the four-site TIP4P model but the parameters are adapted to
175 yield a better phase transition behavior. With a melting point of 269.8 ± 0.1 K [37] compared to 229
176 K of TIP4P[38] it is appropriate for the simulated system. To control the pressure inside the
177 simulation box during the production run to 1 bar, an anisotropic Parrinello-Rahman barostat with
178 a coupling constant of 2 fs is applied. After energy minimization, the temperature is set to the
179 desired value using a V-rescale thermostat in the canonical ensemble. Subsequently, the pressure
180 in the isobaric-isothermal ensemble is controlled with a Berendsen barostat. All bonds including
181 hydrogen atoms are constraint with the LINCS[39] algorithm enabling an integration time step of 2
182 fs during the production run.
183 Furthermore, periodic boundary conditions (PBC) are used during the simulation to eliminate
184 boundary effects and to create a defined geometry of regularly distributed AFP molecules.
185 Therefore, the unit cell, which is the simulated system, is duplicated in all three dimensions and
186 placed around the simulation box (Figure 3). In Figure 3 A) the principle of PBC is exemplarily
187 shown in two dimensions for the yellow molecule. Due to the periodic boundary the yellow atom,
188 which leaves the simulation box at the right side, re-enters from the left.
189
190
191

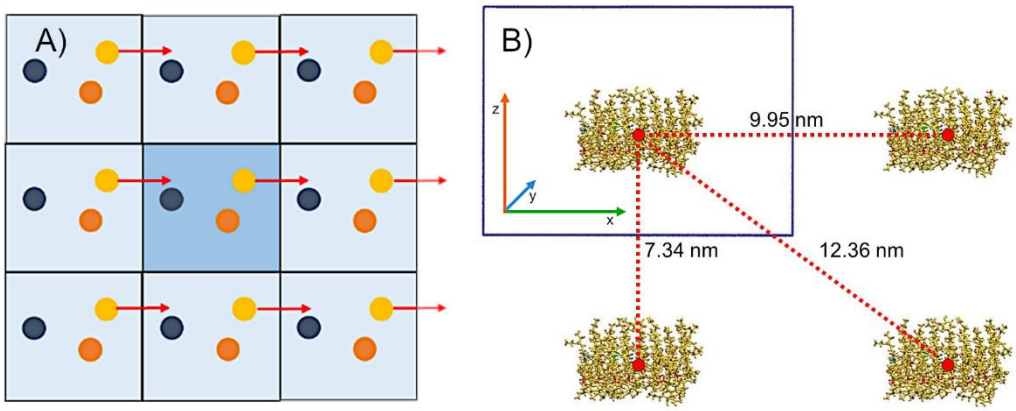

Figure 3. A) Simplified, two dimensional drawing of periodic boundary conditions in MD simulations. The original simulation box is shown in darker blue in the center and contains three example atoms (yellow, orange and dark blue). The simulation box is duplicated and placed around the original simulation box, depicted in light blue. Due to the periodic boundary an atom that leaves the box (yellow at the right side), re-enters from the other side (left). In our case, leaving and entering "atoms" are water molecules. B) Geometry created by connecting four simulation boxes with one adsorbed sbwAFP in each box. The size of the original simulation-box is shown by the blue box. Logically, the distance between the centers of mass of the proteins (red dotted lines) is equal to the corresponding box length in x- and z-direction respectively. The longest distance between AFP in this arrangement is the diagonal with 12.36 nm.

Simulation system

The simulation box with a size of 9.95 nm x 9.98 nm x 7.35 nm in x-, y- and z-direction contains 93560 atoms in total, whereof 1760 water molecules are restraint as a single ice layer (Figure 4 A)). Since it is highly unlikely that water will start crystallizing under the simulation conditions, this ice layer functions as a seed crystal to promote ice crystal growth. To ensure binding of the insect AFP, the ice layer is able to grow freely in direction of the secondary prism plane and the AFP is oriented with its ice-binding site towards the ice front. A slab of 919 restraint water

210 molecules prevents the growth of ice to the lower direction, which has to be avoided since three-
211 dimensional periodic boundary conditions are applied. The simulated sbwAFP (Figure 4 B))
212 (RCSB: 1M8N) is a hyperactive insect AFP which is able to bind to the secondary prism plane and
213 the basal plane[22,40]. Kuiper et al. already demonstrated that this specific AFP is able to bind to the
214 secondary prism plane of a growing ice crystal in a MD simulation[28].

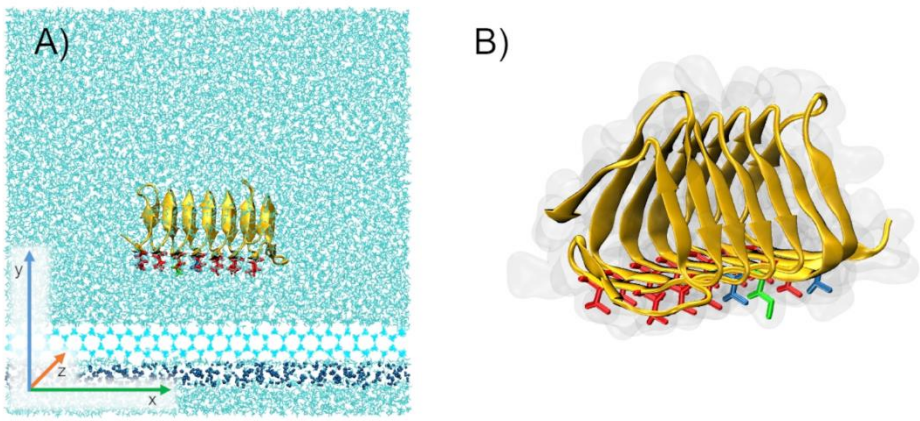

215

216 **Figure 4.** A) Starting configuration of the system. The spruce budworm AFP is placed in the center
217 and the ice-binding site is oriented towards the fixed ice layer (light blue). In addition, a fixed layer
218 of water molecules (blue dots) is introduced to prevent ice growth in the down direction. Finally,
219 the box is filled with water molecules (turquoise). B) Spruce budworm AFP visualized as a cartoon
220 drawing (yellow). For a better representation of the ice-binding site, the corresponding amino acids
221 are shown as licorice representation and in different colors. Threonine residues are depicted in red,
222 valine in blue and isoleucine in green. To get an impression of the dimension, the surface is
223 indicated as grey shadow.

224 **Determination of T_{Min} after binding of sbwAFP**

225 The temperature T_{Min} is defined here as the lowest temperature at which the system does not
226 freeze completely. To determine T_{Min}, the box is simulated at different temperatures below the

melting point and the state of the system is observed. In addition to the visual assessment if the system is freezing or not, the progression of the density is examined to see density changes due to the ice growing. Moreover, the simulation with the lowest temperature, which remains in a liquid state, was repeated three times in total and extended to 300 ns. The results are shown in Table 2. These simulations will be abbreviated in the further course of this paper as Sim 1, Sim 2 and Sim 3.

Visualization of the ice surface and determination of the curvatures radius

For the visualization of the ice surface and for the examination of the radius of curvature of the ice crystal in between the bound molecules slabs are cut out the simulation box in several directions. The advantage of using slabs is that the desired plane is visualized without superimposition of water molecules in the planes behind and in front. An easy and fast method to create those slabs is the use of the clipping plane tool in VMD. This tool allows cutting the three-dimensional box along a plane which is defined by its vector and slabs with a thickness of 0.7 – 1 nm are created. Hence, the cuts can be set freely within the simulation box, it is possible to obtain horizontal (xz plane) and vertical (yz plane) slabs. The horizontal slabs provide an overview of the ice surface and allow the identification of the geometry of the ice surface landscape. To visualize the curvature of the ice surface the vertical slabs are used. All vertical slabs, which are analyzed, are shown in Figure 5 A) and alphabetically numbered. In order to calculate the radius based on the vertical slabs, the chord length s and the height of a circular segment h (Equation 3, Figure 5 B)) are used.

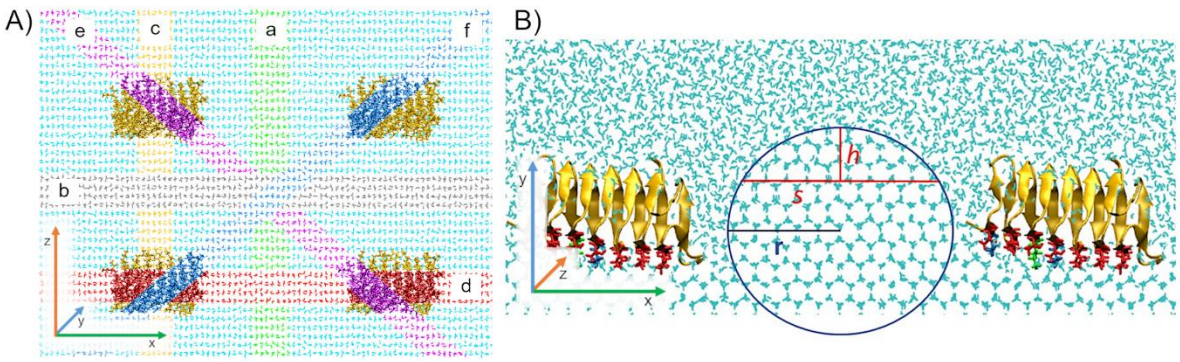

Figure 5. A) Slabs that are generated and observed during the simulation. The slab of the xz plane is shown from the top. B) Exemplary image of slab d (xy plane) viewed from the front of the box. The radius r can be obtained by measuring the length s of the chord and the corresponding height h.

Equation 3. Calculation of the radius of a circular segment

$$r = \frac{4h^2 + s^2}{8h}$$

The precision of this method is estimated by calculating the radius three times at different heights and chord lengths. Those radii result in three melting temperatures $T_m(x)$ according to the Gibbs-Thomson equation. The greatest deviations occur when a clear phase boundary cannot be identified. Taking this into account, the largest measured standard deviation is 0.574 K of 96 slabs in total. To get a better overview over the deviation of this method, the smallest deviation and the third quartile are determined which states that 75 % of all deviations are less than or equal to this value. They are 0.007 K and 0.234 K, respectively. Moreover, the deviation of the individual temperature ranges is far greater than the standard deviation caused by the determination method. In conclusion, we can state that the performed determination method is a simple and quick analysis with adequate accuracy. An alternative would be the calculation and usage of an order parameter to create an artificial cutoff for the separation between ice and water. However, the selection of

the cutoff value itself can influence the structure of ice surface, especially since it is a highly dynamic interface and the computational time increases drastically for the analysis.

Depending on the ice surface geometry, the Gibbs-Thomson equation is adapted resulting in Equation 4 for a cylindrical and Equation 5 for an arbitrary elliptical geometry. Subsequently, the mean value and the corresponding standard deviation are calculated. When using two different radii in the Gibbs-Thomson equation (Equation 5), the average value of the radii is used.

The radii depend on the dynamic and the geometry of the ice surface. Since the simulation at T_{Min} is repeated three times, a static evaluation at fixed times is performed to analyze differences between identical starting setups. In addition to the static analysis, a dynamic analysis of the radii is carried out. Here, the radii are measured over the course of the simulation whenever the curvature is at its maximum.

Calculation of the expected TH with the Gibbs-Thomson equation

With the calculated radii of curvature, the expected depression of the melting temperature $T_m(x)$ is calculated with the Gibbs-Thomson equation (Equation 1). The parameters used are shown in Table 1. They depend on the used water model and are specific for the pyramidal plane bound by the AFP in the simulation. Depending on the geometry of the ice surface, the geometry factor of the Gibbs-Thomson equation is adapted. The depressed melting temperature $T_m(x)$ of a cylindrical surface with radius r can be calculated according to Equation 4.

Table 1. TIP4P/Ice parameters

Property	Value
Bulk melting temperature T_m^∞ [37]	269.8 K
Surface tension of the secondary prism plane σ [41]	0.0316 $\frac{J}{m^2}$
Enthalpy of fusion ΔH_f [41]	1.29 $\frac{kcal}{mol}$ or 5397.36 $\frac{J}{mol}$
Density of TIP4P/Ice ice [37]	906 $\frac{kg}{m^3}$
Molecular weight of water and ice M	0.018 $\frac{kg}{mol}$

Equation 4. Gibbs-Thomson equation for a cylindrical surface geometry

$$T_m(x) = T_m^\infty - \frac{M * \sigma * T_m^\infty}{\rho * \Delta H_f * r}$$

Whereas $T_m(x)$ of an arbitrary elliptical geometry can be calculated with Equation 5. This applies also for a spherical structure since this is a special case of an ellipse where both radii are of the same length.

Equation 5. Gibbs-Thomson equation for an elliptical surface geometry with principal radii r_1 and r_2

$$T_m(x) = T_m^\infty - \frac{M * \sigma * T_m^\infty}{\rho * \Delta H_f} * \left(\frac{1}{r_1} + \frac{1}{r_2}\right)$$

Since many different slabs were evaluated, the ice crystal surface is analyzed in detail and the critical radius determining the extent of the melting point depression can be identified.

306 RESULTS

307 **Determination of T_{Min} after binding of sbwAFP**

308 For the determination of T_{min} different temperatures were simulated for at least 200 ns. The
309 simulation results were analyzed at first visually and the state of the system was observed.
310 Secondly, a detailed analysis of the density curve was carried out.

311 The starting configuration is identical for each simulation (Figure 6 A)), the protein is oriented
312 with its ice-binding site towards the ice surface and is able to move freely within the box. At the
313 beginning, the ice grows in the y-direction and the distance to the protein becomes smaller. During
314 the first 50 ns, the protein is able to bind to the growing ice crystal. Directly after the binding
315 process, no curvature is visible (Figure 6 B)). Remarkably, the protein binds in each of the eight
316 simulations performed but the binding orientation is slightly different which may influence the ice
317 formation. In some cases, the protein binds parallel to the x-axis and in other cases it is shifted.
318 This can exemplarily be seen in Figure 6 B) and D) where the proteins are shifted on one side in
319 the direction of the y-axis. In contrast, in Figure 6 C) it is bound to the ice surface parallel to the
320 x-axis. An important aspect regarding the binding behavior is the interaction strength between the
321 protein and the ice surface. "AFPs that adsorb strongly will have higher surface concentrations and
322 a larger thermal hysteresis gap" (Kumari et al. 2020, page 2444)[42]. The simulative determination
323 of this interaction strength proves to be difficult, since the dynamic of the ice surface has a non-
324 negligible influence on the adsorption of the protein. This in turn depends on the force field and
325 the water model used. Therefore, a comparison and an estimation of which combination of force
326 field and water model provides the most accurate results or whether the influence of the force
327 fields is not decisive at all should be included in future studies .

After the protein has bound to the ice surface, the ice crystal continues to grow and a curvature is formed. With increasing curvature the radius and thus the melting temperature decreases and the growing ice front is stopped if the set simulation temperature equals with the melting temperature (Figure 6 C)). If the simulation temperature is lower and larger radii of curvature can be formed, the AFP is overgrown and trapped inside the ice crystal (Figure 6 D)).

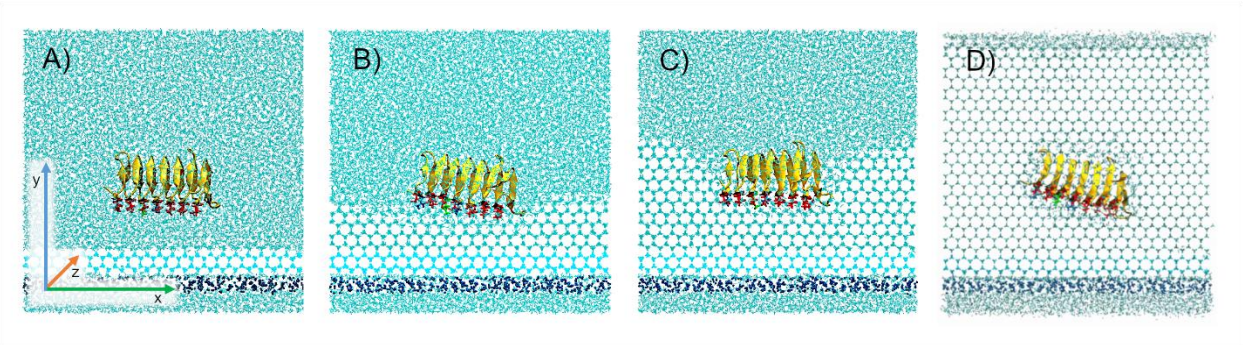

Figure 6. Basic course of the simulation and possible system states. A) Starting configuration, which is the same for all simulations. B) The AFP is able to bind to the growing ice surface. The picture is taken at a temperature of 262.5 K (Sim 3). C) After the binding process, ice continues to grow and a curvature is formed. (262.5 K, Sim 1). D) If the temperature is too low, the protein is overgrown and trapped in the ice (262.2 K). Depending on the actual degree of super cooling the endpoint of the simulation is either C) or D).

According to the visual analysis of the simulation box, the temperature at which the system does not freeze completely is at 262.5 K (Table 2).

Table 2. System state after visual observation at different simulation temperatures

Temperature / K	System state
260	Frozen
261.5	Frozen
262.0	Frozen
262.2	Frozen
262.5	Unfrozen
265	Unfrozen

Besides the visual observation, the density and the height of the ice layers were examined to identify whether the system at the given temperature freezes or not. The development of the density with and without AFP is shown in Figure 7. We assume that the ice growth rate is proportional to the decrease of density. Without AFP, the system freezes within 100 ns at a temperature of 265 K. Due to the inserted ice grid, the density at the start of the simulation is already somewhat lower than for pure water. In the further course of the simulation, the density decreases almost linearly until the box is frozen in the y-direction. In case no AFP is present, a lowest density of 925 kg/m^3 is reached (Figure 7 A)). In contrast, the presence of sbwAFP increases this value to about 935 kg/m^3, assuming that the temperature is low enough for the ice to overgrow the protein (Figure 7 B)). Three phases can be identified that always occur in our simulations when the system with AFP freezes completely. Figure 7 B) shows the density progression of a system at 262.2 K that freezes in the course of the simulation. The three phases are alphabetically numbered from a to c. During phase a, the density decreases linearly due to the ice formation. After binding of the protein, ice growth is impaired and the ice cannot longer grow with a straight surface. The pinning of the ice surface results in a curvature and a reduced ice formation velocity (phase b). This means that

the ice still continues to grow with a curved surface. As long as this curvature is not strong enough to stop the ice growth, the ice is able to grow over the protein and a continuous layer can form. In this case, the growth rate of the ice can increase again as can be seen in phase c. The system then freezes up to a density value of approximately 930 kg/m^3. This relation holds true for all simulations below 262.5 K.

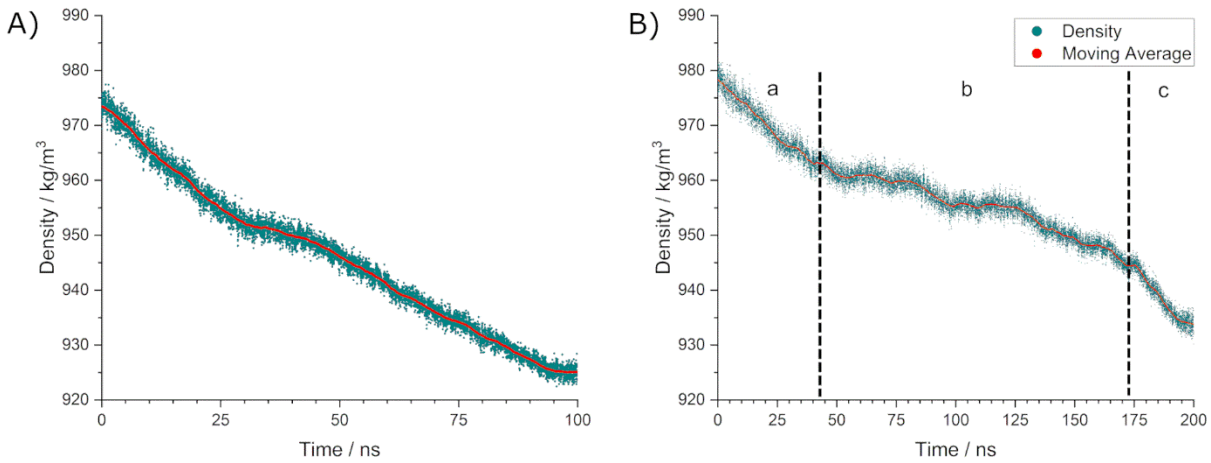

Figure 7. A) Progression of the density at 265 K without AFP. At the beginning, the density is around 975 kg/m^3 and decreases linearly during the simulation. At 95 ns the box is frozen and the density reaches a threshold of 925 kg/m^3. B) System with AFP at a temperature of 262.2 K. The density progression can be divided into three phases a-c. In the first phase (a) from 0 to 45 ns the ice crystal grows and the protein binds to the ice surface. Afterwards, in the second phase (b), the curvature develops but cannot stop the formation of ice. The velocity of the ice formation is reduced. When the protein is engulfed and the first ice layer above the protein is formed, the hindrance of ice formation is lower and thus the ice formation rate increases again. This can be seen in the third phase (c).

At moderate supercooling, the resulting curvature prevents freezing and the course of the density approaches a threshold value. The threshold value depends on temperature, since at higher

temperatures the critical radius of curvature is larger and is therefore reached earlier. This limits the maximum amount of ice in the system. For example, at a temperature of 262.5 K a lowest density of approx. 960 kg/m^3 is reached (Figure 8), whereas at 265 K the density does not decrease below 970 kg/m^3.

The simulation at 262.5 K was repeated three times in total. Hereinafter referred to as Sim 1, Sim 2 and Sim 3. This was done to see differences between individual simulations at the same temperature, to evaluate the impact on the resulting curvature and to make sure that 262.5 K is the critical temperature T_{min}. Figure 8 shows the progression of the density of the three simulations at 262.5 K. Although all simulations have the same initial conditions, the ice formation and therefore the density progression is not identical. One influence that may play a role here is the previously mentioned slightly different binding configuration of the protein. For Sim 1 and Sim 2 the course of the density is quite similar. It reaches apparently a constant value around 150 ns but afterwards it decreases again. Even though a longer simulation might have led to an overgrowth of the protein, this could not be observed in the simulations presented here. In contrast, Sim 3 approaches the threshold slightly above 960 kg/m^3 and stays constant for the rest of the 450 ns of the simulation. To ensure that the density reached a constant value, the simulation was extended from 300 ns to 450 ns. The initial ice formation seems to be the same for all three simulations, since the density converges to a value of 960 kg/m^3 during the first 150 ns. In this context, the simulation time needed to produce reliable information is important. As seen in the density progressions of Sim 1 and Sim 2, the system would have been stable at around 150 ns without further simulation. This may lead to wrong assumptions when systems with antifreeze molecules are simulated in a too short range. This shows the principal need of relatively long simulation times for well-founded statements.

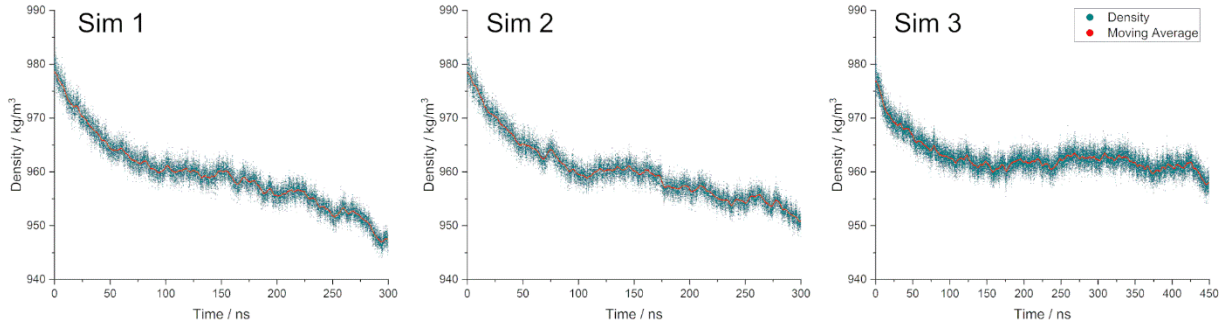

Figure 8. Density progression of the three simulations at 262.5 K. The first two simulations, Sim 1 (left) and Sim 2, (middle) seem to reach a threshold around 150 ns, but the density continues to decrease in the further course of the simulation. Sim 3 (right), is stable at a density around 960 kg/m^3 for a simulation period of 450 ns.

We can conclude from the detailed simulation analyses that the lowest temperature at which the system does not freeze completely is close to $T_{min} \approx 262.5\ K$. Hence, Sim 1 and Sim 2 tend to freeze for longer simulation times; the temperature T_{min} may be slightly higher. These three simulations are analyzed in more detail below for the surface geometry and the different radii.

Pre-analysis of the three dimensional ice surface at T_{min}

Before the critical radius can be determined, the general structure of the ice surface needs to be examined. A good way to get an overview over the geometry of the ice surface is to analyze horizontal (xz plane) slabs through the simulation box (Figure 9). Because of its regular structure, ice can easily be distinguished from the disordered water molecules. All three simulations at 262.5 K show the same cylindrical ice pattern at the surface.

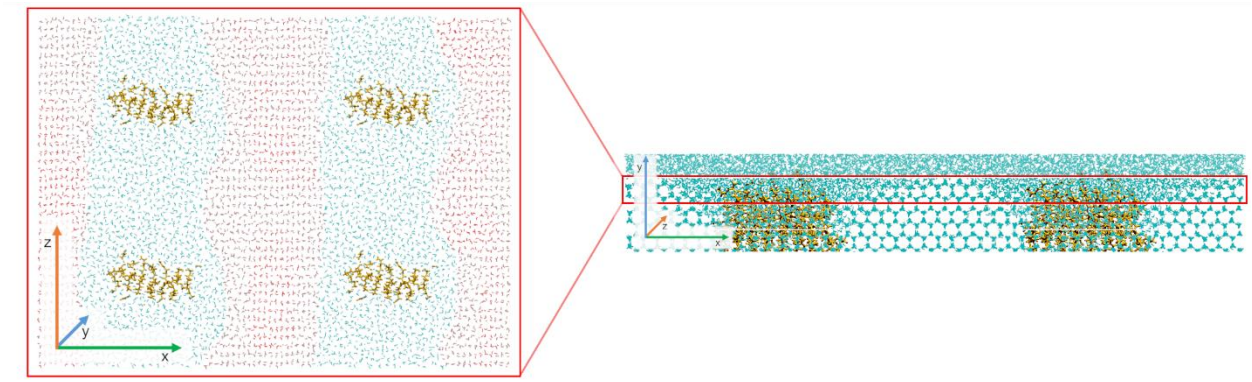

Figure 9. Top view of a horizontal slice to visualize the geometry of the ice surface. The water molecules are roughly divided into ice (red) and water (cyan). To spatially classify the slice, the front view of the box is depicted on the right.

To make the cylindrical shape obvious, the length axis of the cylinder is analyzed with the help of slab a (Figure 5 A)). No curvature can be identified in the z-direction of slab a during all simulations and at different simulation times (Figure 10).

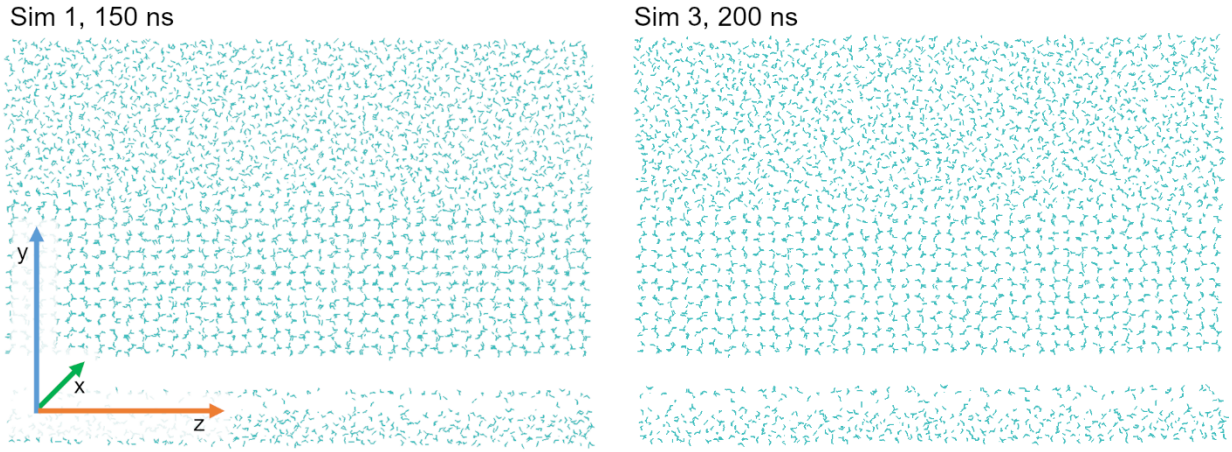

Figure 10. Slab a of two different simulations at different time points. Both slices show a straight ice surface. This is also true for Sim 2 and other times. It is worth mentioning, that no curvature is formed despite the fact that the ice layer grows.

Due to the shape of the surface, the critical radius, which determines the depression of the melting temperature, has to be on the cylinder and perpendicular to the longitudinal axis (z - direction). In addition, it can be seen from Figure 9 that the cylinder is not exactly uniformly shaped and different curvature radii are present in the x-direction. The shortest radius is directly between the two AFP molecules and corresponds to slab d, whereas slab b is located at the widest point of the cylinder (Figure 5 A)). Again, this is the same for all three simulations.

Analysis of the radii of curvature and calculation of $T_m(x)$ with Gibbs-Thomson equation

Now the different radii are determined and inserted into the Gibbs-Thomson equation. In this way, the expected melting temperature $T_m(x)$ at this location is determined. In the case of the critical radius, this should correspond to the temperature T_{min} already determined. The geometry of the ice surface plays a critical role in the calculation of $T_m(x)$ with the Gibbs-Thomson equation. As already shown, a cylindrical surface between the proteins with a longitudinal axis in z-direction can be seen and one may assume that the critical radius is to be found on the cylinder perpendicular to the longitudinal axis. We investigated this aspect in more detail for the three simulations Sim 1, Sim 2 and Sim 3 at T_{min} = 262.5 K. Therefore, all reasonable radii in the system are examined, not only those on the cylinder. First, the static analysis at specific time points provides information about the temporal behavior of the various radii in the system. For example, radii which are permanently very short can be neglected, since the resulting melting temperature $T_m(x)$ at this point is always below the ambient temperature. Second, the radii that cannot be excluded are subjected to a dynamic analysis in which they are measured at maximum curvature.

Static analysis

At first, the slabs c and d directly between the proteins are examined (Figure 11). For slab d located between the proteins in x-direction (Figure 11 A)), the cylindrical version of the Gibbs-Thomson equation (Equation 4) can be used. The resulting radii of curvature (Table S1) are comparably short and the melting temperature is below the ambient temperature (Table 3).

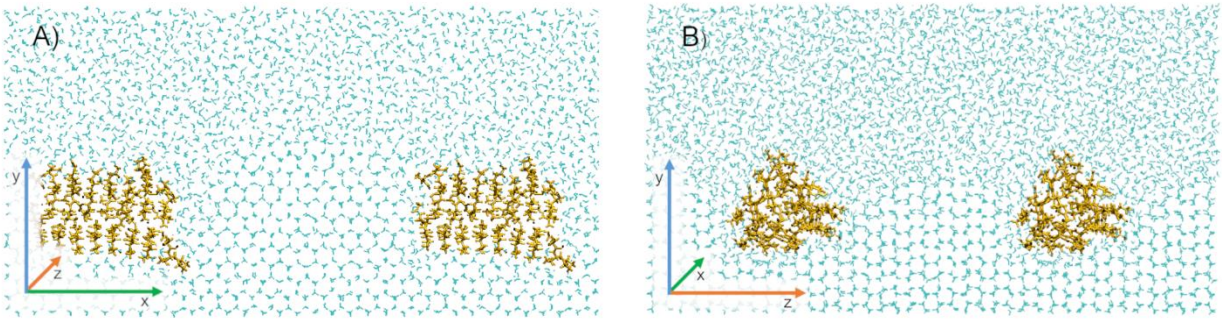

Figure 11. A) Slab d of Sim 2 at 200 ns. The ice surface between the proteins is strongly curved and the top of the ice surface is slightly above the protein. B) Slab c of Sim 1 at 175 ns. The height of the curvature is lower and below the height of the protein.

In contrast, slab c between the proteins in z-direction (Figure 11 B)) is not part of the cylindrical surface geometry and therefore the cylindrical geometry factor cannot be used. For the calculation of the melting temperature with Equation 5 we need the radius of curvature perpendicular to slab c in x-direction. This is delivered by the surface analysis of slab b (Figure 12).

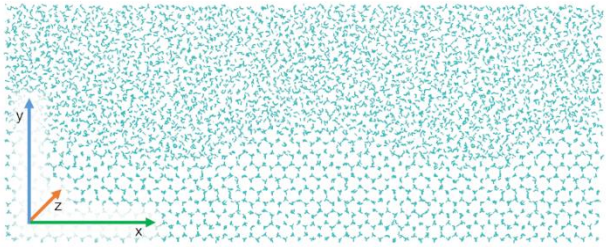

Figure 12. Slab b of Sim 3 at 200 ns. In the center the curvature has formed, which leads to negative curvatures flanking the elevation in the center. The minima of these negative curvatures are between the proteins in z-direction.

It turns out that a minimum height of the ice surface with a negative radius of slab b is directly between the proteins. For the calculation of the corresponding melting temperature, Equation 5 was used with the two perpendicular radii at the crossing section (c and b). As the radius in x-direction is negative, the calculation of melting temperatures leads to comparably high melting temperatures (Table 3). Due to the negative radius there is a high tendency for water molecules to adsorb to the surface at this point. Nevertheless, by filling this area the radius increases to zero (flat surface) and the radius in z-direction dominates the melting temperature. Yet the radius in z-direction is too small to be the critical radius. One can see this by elaboration of the measured radii for different simulation times (Table S2). For these reasons we assume that the critical radius cannot be located at this position.

Table 3. Melting temperatures according to the Gibbs-Thomson equation at slab c and d at 200 ns. Ambient temperature is 262.5 K

Simulation	Time / ns	Slab	Temperature $T_m(x)$ / K
1	200	d	261.47 ± 0.36
2	200	d	261.15 ± 0.49
3	200	d	262.10 ± 0.17
1	200	b+c	262.63
2	200	b+c	270.79
3	200	b+c	266.87

A similar problem arises for the diagonals, slab e and f. They are located at the cylinder but to use the cylindrical Gibbs-Thomson equation, they need to be perpendicular to the length axis of the cylinder. If Equation 4 is used erroneously, the radii will be incorrectly prolonged leading to an unfeasible high melting temperature as show in Table 4. On the other hand, one can state that

slab e and f are approximately perpendicular and calculate the melting temperature with these two radii and Equation 5. This results in comparably low values for the melting temperature (Table 5) and thus provides evidence that in this system the longest distance between the proteins is not decisive for the melting point depression.

Table 4. Melting temperature of slab e and f, calculated with the cylindrical Gibbs-Thomson equation (Equation 4)

Simulation	Time / ns	Slab	Temperature $T_m(x)$ / K
1	200	e	264.64 ± 0.16
2	200	e	263.42 ± 0.31
3	200	e	264.58 ± 0.19
1	200	f	264.22 ± 0.24
2	200	f	263.70 ± 0.09
3	200	f	264.37 ± 0.13

Table 5. Corresponding melting temperatures of slab e and f, calculated with the elliptical Gibbs-Thomson equation (Equation 5)

Simulation	Time / ns	Slab	Temperature $T_m(x)$ / K
1	200	e+f	259.07
2	200	e+f	257.33
3	200	e+f	259.16

The last slab to be analyzed is the most promising, which is slab b. It is perpendicular to the longitudinal axis and at the same time the widest point of the cylinder along slab a. In addition, the usage of the cylindrical Gibbs-Thomson equation is perfectly applicable in that case.

As seen in Table 6 most of the calculated melting temperatures are above T_{min} =262.5 K. This means that the curvature would still be able to grow and the maximum melting point depression is not reached yet.

Table 6. Resulting temperature range for the melting point at the position of slice b at fixed times

Simulation	Time / ns	Slice	Temperature $T_m(x)$ / K
1	175	b	262.97 ± 0.18
1	200	b	265.52 ± 0.12
2	175	b	264.18 ± 0.17
2	200	b	265.50 ± 0.32
3	175	b	265.63 ± 0.08
3	200	b	264.98 ± 0.01

Only the melting temperature $T_m(x)$ at 175 ns in Sim1 seems to be in the right order of magnitude. In addition, these values suggest that there are large differences between the simulations. However, keeping in mind that the ice surface is in a dynamic equilibrium it is not surprising that the radii of curvature are changing over time and cannot be expected to be the same between different simulations at fixed times. It can be concluded from the static analysis that the individual simulations show differences and therefore fixed time points cannot be directly compared with each other. Although the overall ice formation seems to be similar based on the density curves, the formation and variation of the curvature develops is different in each simulation. The curvature may be formed the same way with a similar radius, but this is coincidence for a fixed time point. Another reason for the deviations of the three simulations at 262.5 K may be the slightly different binding orientations of the AFP since this could have an

impact on the ice formation and the surface topology. Therefore, a dynamic analysis of the most promising surface area of slab b is shown in the next chapter.

Dynamic analysis

In the dynamic analysis, the development of slab b was examined throughout the simulation. During the simulation time, the ice curvature at slab b builds up until a certain extent but then starts to melt again (Figure 13). This happens repetitively throughout all simulations and during the whole simulation time showing impressively the dynamic equilibrium. In contrast, the curvature of all other slabs is formed without the curvature melting away completely and may be approximated as continuously growing until the maximum curvature is reached. This does not mean that the ice surface here is rigid and that there is no dynamic equilibrium between melting and freezing. Nevertheless, it stands out that the ice formation and the ice surface in slab b is far more dynamic than in the other slabs.

The ice formation at the position of slice b was recorded and the radius of curvature was determined whenever it reaches a maximum. This should yield a melting temperature in the range of the previously determined T_{min}.

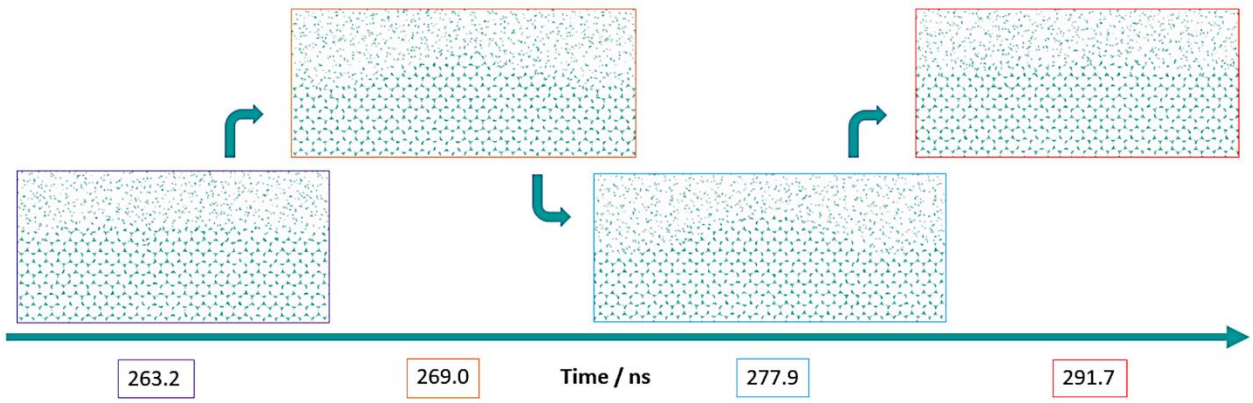

Figure 13. Formation of the curvature between 263 and 292 ns at slab b (yz plane) of Sim 3. At 263 ns, no curvature is visible. In the further course of the simulation, the curvature starts to form and is stable for around 20 ns. During this time, minor fluctuations happen, but no significant growth or melting is observed. After 30 ns, the curvature is completely melted and the ice formations starts again to form a new curvature.

The resulting melting temperatures $T_m(x)$ shown in Table 7 were calculated with the cylindrical Gibbs-Thomson equation (Equation 4). They are very close to the observed T_{min} of 262.5 K. However, the values tend to be somewhat higher which would be in agreement with the previous observation that Sim 1 and Sim 2 could freeze during longer simulations.

Table 7. Melting point at position b determined at maximum curvature

Simulation	Time / ns	Slice	Temperature $T_m(x)$ / K
1	172.7	b	263.21 ± 0.29
2	122.9	b	262.75 ± 0.09
2	178.9	b	262.46 ± 0.22
3	217.2	b	262.94 ± 0.08

549 Because of these findings, we assume that the critical radius is located at the position of slab b.
550 To summarize the results of the dynamic analysis, it can be said that the length of the radii and the
551 resulting melting temperatures at slab b are in very good agreement with T_{min}. It is noteworthy
552 that the critical radius is not found between the proteins and is located on the free, unoccupied ice
553 crystal surface. Contrary to Naullage et al., the critical radius in our simulation is not located at the
554 widest distance in the distribution since this would be the diagonal between the proteins. Instead,
555 one could say that the critical radius is located at the largest distance of the formed geometric
556 structure on the ice surface.

557 In addition, it is important for us to emphasize once again that the simulations reproduce the
558 Gibbs-Thomson effect well, but a comparison of the simulation with experimentally measured
559 thermal hysteresis is not possible. Reasons for this have already been given, such as the unknown
560 surface occupancy of the AFP on the ice crystal and the distribution of the distances between the
561 proteins, or the fact that the ice growth is only investigated at one specific ice crystal plane. As
562 already mentioned before, the determination of the affinity of the protein to the single crystal
563 surface is of great importance. Due to the specification of the box size, this interaction is not
564 correctly reproduced in the simulation. It is obvious by repeated simulation whether a protein binds
565 better or not, but in the case that it binds, the surface occupancy is predetermined by the box.
566 Therefore, it would be desirable to be able to determine this binding strength unambiguously.
567 Kumari et al. also proposed a new method to compare the adsorption behavior of different AFP or
568 towards different ice crystal planes. This method should be evaluated in more detail. In
569 combination with other MD simulations, this could provide further insights into the functioning of
570 AFP and molecules with similar properties. Furthermore, the current incompatibility of
571 experiments and simulations could be improved in the future.

572 CONCLUSION

573 As a general result of our investigation, we can state that the geometry of ice surface is extremely
574 important and may not be guessed upfront the simulation. Due to the rectangular arrangement of
575 the protein and its images, an ellipsoidal curvature was expected but a cylindrical ice surface has
576 been observed in all simulations on the surface. For this reason, it is not purposeful to estimate a
577 maximum radius just from the distances between the proteins. We showed that the critical radius
578 is on a slab where no protein is adsorbed. By simulating different temperatures, the minimum
579 temperature at which the resulting curvature prevents ice growth was determined and is at T_{min} =
580 262.5 K. This is in good agreement with the value calculated with the Gibbs-Thomson equation at
581 the critical radius. For the identification of the critical radius is important that the simulation time
582 is sufficient and that the dynamics auf the ice front is taken into account. We showed that in our
583 case the critical radius was the most dynamic one and not located at the longest distance between
584 the adsorbed molecules. Therefore, it is necessary to determine this radius over the course of the
585 simulation.

586 Over all, our results show on the one hand that the Gibbs-Thomson effect can be taken as the
587 basis of thermal hysteresis and that MD simulations are suitable for the prediction of the melting
588 point depression. The simulations could provide the possibility to compare different AFP or
589 mutants based on their thermal hysteresis in an identical system with same distances between the
590 proteins. The force field used could also have an influence on the adsorption of the water molecules
591 to the ice structure in the simulation. This should be evaluated in future studies. However, it is still
592 not possible to compare an experimentally determined thermal hysteresis with a value obtained by
593 simulation.

594

SUPPORTING INFORMATION

Table S1. Radii and corresponding melting temperatures of the static analysis calculated with the cylindrical Gibbs-Thomson equation

Simulation	Slab	Time / ns	Radius / nm	Temperature $T_m(x)$ / K
1	b	150	7.63	265.69
1	b	150	7.29	265.50
1	b	150	7.40	265.56
1	b	175	4.51	262.84
1	b	175	4.54	262.89
1	b	175	4.73	263.17
1	b	200	7.10	265.38
1	b	200	7.45	265.59
1	b	200	7.44	265.58
1	c	150	3.75	261.43
1	c	150	3.62	261.12
1	c	150	3.80	261.55
1	c	175	3.24	260.12
1	c	175	3.19	259.97
1	c	175	3.35	260.44
1	c	200	2.62	257.80
1	c	200	2.68	258.08
1	c	200	2.63	257.86
1	d	150	3.65	261.19
1	d	150	3.76	261.45
1	d	150	3.60	261.09

1	d	175	3.14	259.79
1	d	175	3.08	259.61
1	d	175	3.25	260.13
1	d	200	3.64	261.18
1	d	200	3.96	261.87
1	d	200	3.72	261.36
1	e	150	6.87	265.23
1	e	150	6.84	265.22
1	e	150	6.97	265.30
1	e	175	5.53	264.12
1	e	175	5.54	264.14
1	e	175	5.40	263.99
1	e	200	5.94	264.51
1	e	200	6.03	264.60
1	e	200	6.31	264.82
1	f	150	6.18	264.72
1	f	150	5.99	264.56
1	f	150	6.11	264.67
1	f	175	4.89	263.38
1	f	175	5.20	263.76
1	f	175	5.08	263.62
1	f	200	5.51	264.10
1	f	200	5.47	264.06
1	f	200	5.91	264.49
2	b	150	6.87	265.23
2	b	150	7.12	265.39

2	b	150	7.26	265.48
2	b	175	5.78	264.37
2	b	175	5.47	264.06
2	b	175	5.53	264.12
2	b	200	6.74	265.14
2	b	200	7.52	265.63
2	b	200	7.73	265.74
2	c	150	2.99	259.29
2	c	150	3.12	259.73
2	c	150	3.24	260.11
2	c	175	3.18	259.95
2	c	175	3.35	260.43
2	c	175	3.42	260.61
2	c	200	3.72	261.36
2	c	200	3.74	261.40
2	c	200	3.89	261.74
2	d	150	2.63	257.85
2	d	150	2.63	257.86
2	d	150	2.66	258.00
2	d	175	4.24	262.39
2	d	175	4.36	262.60
2	d	175	4.48	262.80
2	d	200	3.49	260.80
2	d	200	3.54	260.93
2	d	200	3.88	261.71
2	e	150	4.53	262.87

2	e	150	4.59	262.96
2	e	150	4.52	262.86
2	e	175	4.56	262.91
2	e	175	4.55	262.91
2	e	175	4.59	262.96
2	e	200	4.71	263.13
2	e	200	4.89	263.38
2	e	200	5.19	263.75
2	f	150	5.02	263.55
2	f	150	4.86	263.35
2	f	150	5.01	263.54
2	f	175	6.12	264.67
2	f	175	6.48	264.96
2	f	175	5.91	264.49
2	f	200	5.06	263.59
2	f	200	5.21	263.78
2	f	200	5.16	263.71
3	b	150	6.05	264.61
3	b	150	6.23	264.76
3	b	150	6.37	264.88
3	b	175	7.42	265.57
3	b	175	7.49	265.61
3	b	175	7.69	265.72
3	b	200	6.52	264.98
3	b	200	6.52	264.99
3	b	200	6.50	264.97

3	c	150	3.28	260.22
3	c	150	3.71	261.34
3	c	150	3.57	261.00
3	c	175	2.79	258.57
3	c	175	2.95	259.16
3	c	175	2.86	258.83
3	c	200	3.15	259.83
3	c	200	3.39	260.54
3	c	200	3.14	259.82
3	d	150	3.15	259.84
3	d	150	3.27	260.21
3	d	150	3.45	260.70
3	d	175	3.19	259.96
3	d	175	3.31	260.31
3	d	175	3.40	260.56
3	d	200	4.01	261.98
3	d	200	4.04	262.04
3	d	200	4.18	262.29
3	e	150	6.43	264.92
3	e	150	6.40	264.89
3	e	150	6.48	264.95
3	e	175	5.85	264.43
3	e	175	6.08	264.63
3	e	175	5.90	264.48
3	e	200	5.82	264.40
3	e	200	6.00	264.57

3	e	200	6.25	264.78
3	f	150	5.71	264.31
3	f	150	5.75	264.34
3	f	150	5.72	264.31
3	f	175	5.89	264.47
3	f	175	6.16	264.70
3	f	175	6.32	264.84
3	f	200	5.71	264.31
3	f	200	5.94	264.52
3	f	200	5.69	264.28

Table S2. Radii and melting temperatures when slab c and b are combined. For the calculation, the elliptical Gibbs-Thomson equation is used.

Simulation	Time / ns	Average radius for slab b / nm	Average radius for slab c / nm	Temperature $T_m(x)$ / K
1	150	-3.09	3.72	271.51
1	175	-4.05	3.26	267.94
1	200	-6.65	2.64	262.63
2	150	-4.70	3.11	266.40
2	175	-4.68	3.32	267.05
2	200	-3.38	3.78	270.79
3	150	-4.67	3.52	267.59
3	175	-4.65	2.87	265.61
3	200	-4.61	3.23	266.87

603 **Table S3.** Radii and melting temperatures when slab e and f are combined. For the calculation, the

604 elliptical Gibbs-Thomson equation is used.

Simulation	Time / ns	Average radius for slab e / nm	Average radius for slab f / nm	Temperature $T_m(x)$ / K
1	150	6.89	6.09	260.10
1	175	5.49	5.06	257.88
1	200	6.09	5.63	259.07
2	150	4.55	4.96	256.58
2	175	4.57	6.17	257.84
2	200	4.93	5.14	257.33
3	150	6.43	5.73	259.44
3	175	5.94	6.12	259.39
3	200	6.02	5.78	259.16

605

606 **Table S4.** Radii and corresponding melting temperatures at the position of slab b during the

607 dynamic analysis. The melting temperatures are calculated with the cylindrical version of the

608 Gibbs-Thomson equation

Simulation	Slab	Time / ns	Radius / nm	Temperature $T_m(x)$ / K
1	b	93	4.86	263.34
1	b	93	4.65	263.05
1	b	93	4.79	263.25
1	b	117.1	6.00	264.57
1	b	117.1	5.68	264.28
1	b	117.1	5.69	264.28
1	b	172.7	4.82	263.29

1	b	172.7	4.54	262.89
1	b	172.7	4.93	263.44
1	b	218.6	5.08	263.62
1	b	218.6	5.17	263.73
1	b	218.6	5.05	263.59
1	b	262.1	6.73	265.13
1	b	262.1	7.19	265.44
1	b	262.1	6.93	265.27
2	b	91.9	7.42	265.57
2	b	91.9	7.32	265.51
2	b	91.9	7.12	265.39
2	b	93.7	5.19	263.76
2	b	93.7	4.99	263.51
2	b	93.7	4.96	263.48
2	b	111.6	6.94	265.28
2	b	111.6	6.83	265.21
2	b	111.6	6.84	265.21
2	b	122.9	4.47	262.78
2	b	122.9	4.39	262.65
2	b	122.9	4.49	262.82
2	b	178.9	4.42	262.71
2	b	178.9	4.16	262.26
2	b	178.9	4.25	262.42
2	b	238.2	5.60	264.19
2	b	238.2	5.54	264.13
2	b	238.2	5.65	264.25

2	b	263.9	6.17	264.71
2	b	263.9	5.89	264.47
2	b	263.9	6.11	264.66
3	b	81.8	4.11	262.17
3	b	81.8	4.14	262.23
3	b	81.8	4.13	262.21
3	b	96.4	5.76	264.36
3	b	96.4	5.55	264.14
3	b	96.4	5.82	264.40
3	b	131.0	4.92	263.42
3	b	131.0	5.03	263.56
3	b	131.0	4.91	263.41
3	b	191.1	5.21	263.78
3	b	191.1	5.50	264.09
3	b	191.1	5.03	263.55
3	b	217.2	4.52	262.86
3	b	217.2	4.58	262.94
3	b	217.2	4.64	263.03
3	b	236.2	6.12	264.67
3	b	236.2	6.24	264.77
3	b	236.2	6.57	265.02
3	b	348.8	4.96	263.47
3	b	348.8	4.77	263.22
3	b	348.8	4.73	263.16
3	b	365.7	5.56	264.15
3	b	365.7	5.51	264.10

3	b	365.7	5.53	264.13
3	b	382.5	5.97	264.54
3	b	382.5	5.92	264.50
3	b	382.5	6.12	264.67
3	b	401.7	6.87	265.23
3	b	401.7	6.51	264.98
3	b	401.7	6.70	265.12

611 REFERENCES

612 (1) Davies, P. L. Ice-binding proteins: a remarkable diversity of structures for stopping and
613 starting ice growth. Trends in biochemical sciences **2014**, 39, 548–555.

614 (2) Duman, J. G. Antifreeze and ice nucleator proteins in terrestrial arthropods. Annual review
615 of physiology **2001**, 63, 327–357.

616 (3) Bredow, M.; Walker, V. K. Ice-Binding Proteins in Plants. Frontiers in plant science **2017**,
617 8, 2153.

618 (4) Muñoz, P. A.; Márquez, S. L.; González-Nilo, F. D.; Márquez-Miranda, V.; Blamey, J. M.
619 Structure and application of antifreeze proteins from Antarctic bacteria. Microbial cell factories
620 **2017**, 16, 138.

621 (5) Muldrew, K.; McGann, L. E. Mechanisms of intracellular ice formation. Biophysical journal
622 **1990**, 57, 525–532.

623 (6) Białkowska, A.; Majewska, E.; Olczak, A.; Twarda-Clapa, A. Ice Binding Proteins: Diverse
624 Biological Roles and Applications in Different Types of Industry. Biomolecules **2020**, 10.

625 (7) DeVries, A. L. Glycoproteins as Biological Antifreeze Agents in Antarctic Fishes. Science
626 **1971**, 1152–1155.

627 (8) Raymond, J. A.; DeVries, A. L. Adsorption inhibition as a mechanism of freezing resistance
628 in polar fishes. Proceedings of the National Academy of Sciences of the United States of America
629 **1977**, 74, 2589–2593.

630 (9) Celik, Y.; Graham, L. A.; Mok, Y.-F.; Bar, M.; Davies, P. L.; Braslavsky, I. Superheating of
631 ice crystals in antifreeze protein solutions. Proceedings of the National Academy of Sciences of
632 the United States of America **2010**, 107, 5423–5428.

633 (10) Hanada, Y.; Nishimiya, Y.; Miura, A.; Tsuda, S.; Kondo, H. Hyperactive antifreeze protein
634 from an Antarctic sea ice bacterium Colwellia sp. has a compound ice-binding site without
635 repetitive sequences. The FEBS journal **2014**, 281, 3576–3590.

636 (11) Scotter, A. J.; Marshall, C. B.; Graham, L. A.; Gilbert, J. A.; Garnham, C. P.; Davies, P. L.
637 The basis for hyperactivity of antifreeze proteins. Cryobiology **2006**, 53, 229–239.

638 (12) Bar Dolev, M.; Braslavsky, I.; Davies, P. L. Ice-Binding Proteins and Their Function.
639 Annual review of biochemistry **2016**, 85, 515–542.

640 (13) Olijve, L. L. C.; Meister, K.; DeVries, A. L.; Duman, J. G.; Guo, S.; Bakker, H. J.; Voets,
641 I. K. Blocking rapid ice crystal growth through nonbasal plane adsorption of antifreeze proteins.
642 Proceedings of the National Academy of Sciences of the United States of America **2016**, 113,
643 3740–3745.

644 (14) Davies PL, H. C. L. Biochemistry of fish antifreeze proteins. FASEB J. **1990**, 2460–2468.

645 (15) Martino, M. N.; Zaritzky, N. E. Ice recrystallization in a model system and in frozen muscle
646 tissue. Cryobiology **1989**, 26, 138–148.

647 (16) Bevilacqua, A. E.; Zaritzky, N. E. Ice Recrystallization in Frozen Beef. J Food Science
648 **1982**, 47, 1410–1414.

649 (17) Knight CA, DeVries AL, Oolman LD. Fish antifreeze protein and the freezing and
650 recrystallization of ice. Nature **1984**, 15–21.

651 (18) Gaukel, V.; Leiter, A.; Spieß, W. E.L. Synergism of different fish antifreeze proteins and
652 hydrocolloids on recrystallization inhibition of ice in sucrose solutions. Journal of Food
653 Engineering **2014**, 141, 44–50.

654 (19) Knight C. A., DeVries A. L. Melting Inhibition and Superheating of ice by an AFGP.
655 Science **1989**, 505–507.

656 (20) Jackson, C. L.; McKenna, G. B. The melting behavior of organic materials confined in
657 porous solids. The Journal of chemical physics **1990**, 93, 9002–9011.

658 (21) Basu, K.; Garnham, C. P.; Nishimiya, Y.; Tsuda, S.; Braslavsky, I.; Davies, P. Determining
659 the ice-binding planes of antifreeze proteins by fluorescence-based ice plane affinity. Journal of
660 visualized experiments : JoVE **2014**, e51185.

661 (22) Pertaya, N.; Marshall, C. B.; Celik, Y.; Davies, P. L.; Braslavsky, I. Direct visualization of
662 spruce budworm antifreeze protein interacting with ice crystals: basal plane affinity confers
663 hyperactivity. Biophysical journal **2008**, 95, 333–341.

664 (23) Ramløv, H.; DeVries, A. L.; Wilson, P. W. Antifreeze glycoproteins from the antarctic fish
665 Dissostichus mawsoni studied by differential scanning calorimetry (DSC) in combination with
666 nanolitre osmometry. Cryo letters **2005**, 26, 73–84.

667 (24) Gaede-Koehler, A.; Kreider, A.; Canfield, P.; Kleemeier, M.; Grunwald, I. Direct
668 measurement of the thermal hysteresis of antifreeze proteins (AFPs) using sonocrystallization.
669 Analytical chemistry **2012**, 84, 10229–10235.

670 (25) Hassa-Roudsari, M.; Goff, H. D. A new quantitative method to measure activity of ice
671 structuring proteins using differential scanning calorimetry. Cryo letters **2012**, 33, 118–125.

672 (26) Drori, R.; Davies, P. L.; Braslavsky, I. Experimental correlation between thermal hysteresis
673 activity and the distance between antifreeze proteins on an ice surface. RSC Adv. **2015**, 5, 7848–
674 7853.

675 (27) Weng, L.; Stott, S. L.; Toner, M. Molecular Dynamics at the Interface between Ice and
676 Poly(vinyl alcohol) and Ice Recrystallization Inhibition. Langmuir : the ACS journal of surfaces
677 and colloids **2018**, 34, 5116–5123.

678 (28) Kuiper, M. J.; Morton, C. J.; Abraham, S. E.; Gray-Weale, A. The biological function of an
679 insect antifreeze protein simulated by molecular dynamics. eLife **2015**, 4.

680 (29) Nada, H.; Furukawa, Y. Antifreeze proteins: computer simulation studies on the mechanism
681 of ice growth inhibition. Polym J **2012**, 44, 690–698.

682 (30) Naullage, P. M.; Qiu, Y.; Molinero, V. What Controls the Limit of Supercooling and
683 Superheating of Pinned Ice Surfaces? The journal of physical chemistry letters **2018**, 9, 1712–
684 1720.

685 (31) Midya, U. S.; Bandyopadhyay, S. Operation of Kelvin Effect in the Activities of an
686 Antifreeze Protein: A Molecular Dynamics Simulation Study. The journal of physical chemistry.
687 B **2018**, 122, 3079–3087.

688 (32) Nada, H.; Furukawa, Y. Growth inhibition at the ice prismatic plane induced by a spruce
689 budworm antifreeze protein: a molecular dynamics simulation study. Physical chemistry chemical
690 physics : PCCP **2011**, 13, 19936–19942.

(33) Berendsen, H.J.C.; van der Spoel, D.; van Drunen, R. GROMACS: A message-passing parallel molecular dynamics implementation. Computer Physics Communications **1995**, 91, 43–56.

(34) Humphrey, W.; Dalke, A.; Schulten, K. VMD: Visual molecular dynamics. Journal of Molecular Graphics **1996**, 14, 33–38.

(35) Abascal, J. L. F.; Sanz, E.; García Fernández, R.; Vega, C. A potential model for the study of ices and amorphous water: TIP4P/Ice. The Journal of chemical physics **2005**, 122, 234511.

(36) Jorgensen, W. L.; Maxwell, D. S.; Tirado-Rives, J. Development and Testing of the OPLS All-Atom Force Field on Conformational Energetics and Properties of Organic Liquids. Journal of the American Chemical Society **1996**, 118, 11225–11236.

(37) Conde, M. M.; Rovere, M.; Gallo, P. High precision determination of the melting points of water TIP4P/2005 and water TIP4P/Ice models by the direct coexistence technique. The Journal of chemical physics **2017**, 147, 244506.

(38) García Fernández, R.; Abascal, J. L. F.; Vega, C. The melting point of ice Ih for common water models calculated from direct coexistence of the solid-liquid interface. The Journal of chemical physics **2006**, 124, 144506.

(39) Hess, B.; Bekker, H.; Berendsen, H.J.C.; Fraaije, G.E.M. LINCS: A linear constraint solver for molecular simulations. Journal of Computational Chemistry **1997**, 1463–1472.

(40) Chakraborty, S.; Jana, B. Molecular Insight into the Adsorption of Spruce Budworm Antifreeze Protein to an Ice Surface: A Clathrate-Mediated Recognition Mechanism. Langmuir : the ACS journal of surfaces and colloids **2017**, 33, 7202–7214.

(41) Espinosa, J. R.; Vega, C.; Sanz, E. Ice–Water Interfacial Free Energy for the TIP4P, TIP4P/2005, TIP4P/Ice, and mW Models As Obtained from the Mold Integration Technique. J. Phys. Chem. C **2016**, 120, 8068–8075.

(42) Kumari, S.; Muthachikavil, A. V.; Tiwari, J. K.; Punnathanam, S. N. Computational Study of Differences between Antifreeze Activity of Type-III Antifreeze Protein from Ocean Pout and Its Mutant. Langmuir : the ACS journal of surfaces and colloids **2020**, 36, 2439–2448.

AUTHOR INFORMATION

Corresponding Author
Julian Gerhäuser, julian.gerhaeuser@kit.edu, Kaiserstraße 12, 76131 Karlsruhe

Author Contributions

The manuscript was written through contributions of all authors. All authors have given approval to the final version of the manuscript.

ABBREVIATIONS

AFP, antifreeze protein; IBP, ice-binding protein; M, molecular mass; MD, molecular dynamics; PBC, periodic boundary condition; r, radius; sbw, spruce budworm; TH, thermal hysteresis; TmAFP, tenebrio molitor antifreeze protein; VMD, Visual Molecular Dynamics; x, diameter